Epitaxial Zintl aluminide SrAl₄ grown on a LaAlO₃ substrate

Lukas Schlipf,[1] Alexander Slepko,[1] Agham B. Posadas,[1] Heidi Seinige,[1] Ajit Dhamdhere,[2]
Maxim Tsoi,[1] David J. Smith,[2] and Alexander A. Demkov[1,*]

[1]*Department of Physics, The University of Texas at Austin, Austin, Texas 78712, USA*
[2]*Department of Physics, Arizona State University, Tempe, Arizona 85287, USA*

Zintl phases are a class of intermetallic materials that have simultaneously ionic and covalent bonding resulting from charge transfer between two different atomic species. We present a combined first principles and experimental study of Zintl-phase SrAl₄, which is grown in thin film form on the perovskite oxide LaAlO₃ using molecular beam epitaxy. The structural properties are investigated using reflection-high-energy electron diffraction, x-ray diffraction, and cross-section transmission electron microscopy, which reveal relaxed epitaxial island growth. Photoelectron spectroscopy measurements verify the Zintl-Klemm nature of the bonding in the material and are utilized to determine the band offset and the work function of SrAl₄, while transport measurements confirm its metallic behavior. The experimentally observed properties are confirmed using density functional calculations.

PACS number(s): 73.20.−r, 73.40.Ns, 73.30.+y

I. INTRODUCTION

Zintl phases, first characterized in the 1930s, are compounds usually of the form $A_a X_x = (A^{n+})_a [X^{(an/x)-}]_x$, where A is an alkali/alkaline earth metal of group 1 or 2 in the Periodic Table and X is an electronegative metal or semimetal of group 13-15.[1] According to the Zintl-Klemm concept, the active metal A donates valence electrons to the electronegative metal X, which in turn forms a sublattice with covalent character typical for the isovalent element.[2] However, as a result of the charge transfer, Zintl phases also show ionic character, effectively combining both bonding mechanisms. Because of this dual nature of the chemical bonding in Zintl phases, there has been increased interest in these materials for their potential use as thermoelectrics,[3] topological insulators,[4] and heteroepitaxial buffer layers for dissimilar materials.[5] Ideal thermoelectric materials require a combination of good electrical conductivity but poor thermal conductivity together with a high Seebeck coefficient. The covalently bonded anion network in a Zintl material provides the electrical conductivity, while the complicated layered structures with large unit cells decrease the phonon (thermal) conductivity.[3] Zintl phases with strong spin-orbit coupling also make good candidates for topological insulators. The strong covalency of the orbitals near the Fermi level enables strong mixing of states that would normally be at the bottom of the conduction band with states that would normally be at the top of the valence band, with the spin-orbit coupling needed to open up a band gap.[4]

There has been significant interest in the epitaxial integration of functional oxides with semiconductors, especially silicon.[6] However, one faces several problems when performing heteroepitaxy of crystalline oxides on semiconductors, such as the abrupt change of the nature of the chemical bonding across the interface, which often disrupts epitaxy.[7] In semiconductors such as Si, the bonding is mainly covalent, but in perovskite oxides, the bonding exhibits a combination of strongly polar covalent and ionic character. This bonding transition at the oxide-semiconductor interface can result in high interfacial energy, which makes wetting less likely and often prevents a Frank–van der Merwe (layer-

by-layer) growth mode. Developing a path for the epitaxial growth of semiconductors on crystalline oxides could open possibilities for fabricating novel devices.[6] While several different crystalline oxides can be grown on semiconductors, the growth of semiconductors on oxides usually results in polycrystalline growth and/or three-dimensional (3D) growth modes.[8] Several successful attempts have been reported, for example by Bojarczuk *et al.*, using solid phase epitaxy and surfactants to grow (111)-oriented germanium or silicon on $(La_x Y_{1−x})_2 O_3$,[9] and the growth of Si(111)/Gd₂O₃/Si stacks by Osten *et al.*[10,11] An important advance in this field was the realization of so-called crystalline oxide on semiconductors (COS) by McKee *et al.*[12] This group used an interface with the composition of Zintl-phase SrSi₂ with a thickness of one-half monolayer to grow epitaxial SrTiO₃ on silicon substrates.[13] In this sense, Zintl-Klemm interfaces between oxides and semiconductors are ideal candidates to enable wetting, thus minimizing interfacial energy. Such an approach has also been demonstrated for GaAs on SrTiO₃.[5]

In this paper, we consider the Zintl-phase material SrAl₄, which can possibly be used for oxide/semiconductor heteroepitaxy and thermoelectric applications. For this purpose, thin films of SrAl₄ are grown on perovskite oxide LaAlO₃ (LAO) substrates using molecular beam epitaxy (MBE). Aside from crystallographic data, not much is known about the properties of SrAl₄. Only very recently has there been some interest in Mg-Sr-Al alloys containing SrAl₄ for use in the transportation industry.[14] Motivated by this, Zhou *et al.* used first principles density functional theory (DFT) to study the electronic structure and mechanical properties of SrAl₄.[15]

The conventional unit cell of SrAl₄ is shown in Fig. 1. The compound has a tetragonal structure with space group $I4/mmm$ and the experimental lattice constants are $a = b = 4.461$ Å and $c = 11.209$ Å.[16] The unit cell consists of two Sr atoms and eight Al atoms. Two types of Al atoms can be distinguished in the unit cell. Aluminum type 1 at the Wyckoff 4d site has four nearest neighbors, all of Al type 1. Aluminum type 2 at the Wyckoff 4e site has five nearest neighbors, four of aluminum type 1 and one Al type 2. The type 1 aluminum shows the tetrahedral arrangement typically exhibited by group
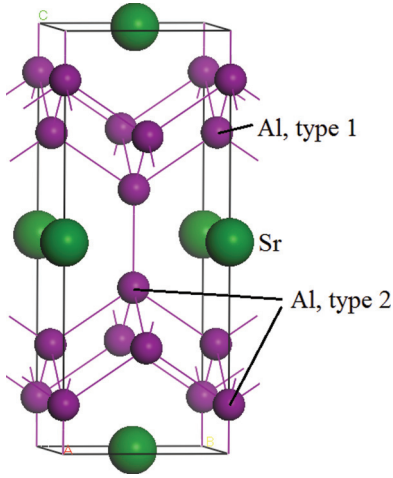
FIG. 1. (Color online) Conventional unit cell of $SrAl_4$.

14 semiconductors such as silicon, with bond angles close to
109.5°. This is an indication of sp^3 hybridization of orbitals
that is typical for semiconductors with four valence electrons.
Hence it can be thought that aluminum, being a group 13
element with three valence electrons, received one electron
from strontium and transformed its bonding characteristics to
that of a group 14 atom. In this simplified view, $SrAl_4$ behaves
in accordance with the Zintl-Klemm concept.

In this work, we have synthesized thin films of $SrAl_4$
by MBE on LAO and characterized them using reflection-
high-energy electron diffraction (RHEED), x-ray diffraction
(XRD), atomic-force microscopy (AFM), and transmission
electron microscopy (TEM). We investigated the electronic
structure and measured the work function using x-ray pho-
toelectron spectroscopy (XPS) and ultraviolet photoelectron
spectroscopy (UPS) and compared these results to DFT
calculations. We also measured resistivity and Hall effect as a
function of temperature using the van der Pauw geometry.

II. THEORY

We use density functional theory (DFT) to calculate the
electronic structure of the Zintl phase $SrAl_4$. We apply the gen-
eralized gradient approximation (GGA) after Perdew, Burke,
and Ernzerhof to estimate the exchange-correlation energy
contribution to the total energy in the Kohn-Sham equation.[17]
To solve the Kohn-Sham equation, we use the plane-wave code
VASP along with PAW pseudopotentials as implemented in
VASP.[18] The valence configuration of Sr is $4s^2 4p^6 5s^2$, and for
Al we use $3s^2 3p^1$. The energy cutoff in the Fourier expansion
of the plane-wave approximation is 500 eV. We found this
energy cutoff to yield sufficiently good convergence in our
previous work on $SrAl_2$.[19] For the Brillouin zone integration,
we use $12 \times 12 \times 6$ and $12 \times 12 \times 2$ Monkhorst-Pack k-
point meshes in bulk and surface calculations, respectively.[20]
In the interface calculation we use a $6 \times 6 \times 2$ k mesh.
With these settings, the theoretical lattice constants are
4.456 Å × 4.456 Å × 11.265 Å, in excellent agreement with
the experimental values of 4.461 Å × 4.461 Å × 11.209 Å.[14]
The energy converged to less than 0.01 meV/cell, and the
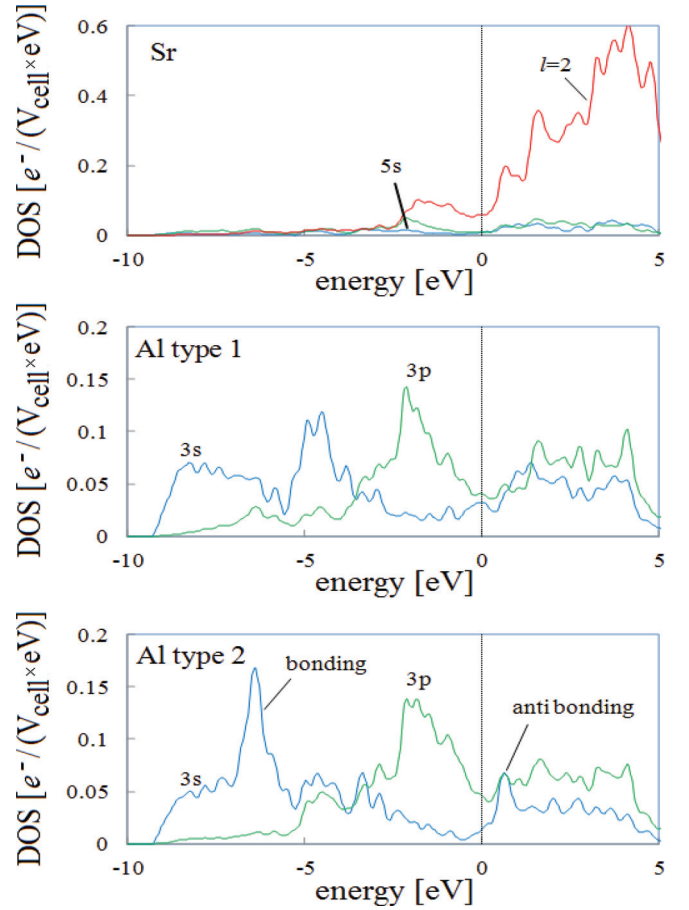
FIG. 2. (Color online) $SrAl_4$ atom and orbital projected electronic
density of states. The Sr semicore states are not shown. Al type 1 and
2 have similar $3p$ energy levels; however, the $3s$ levels differ due to
the formation of one additional bond in type 2 Al.

forces converged to less than 1 meV/Å in the bulk calculation
(~10 meV/Å in surface calculations).

A. $SrAl_4$ bulk

The orbital and atom decomposed electronic density of
states (DOS) are shown in Fig. 2. The semicore Sr $4s$ and $4p$
states appear at -35 eV and -18 eV, respectively (not shown).
The Sr $5s$ states appear between -7 eV and the Fermi level,
and there are additional $l = 1$ and $l = 2$ projections on the Sr
atom between -9 eV and the Fermi level. The Sr conduction
band states are mainly contributed to by $l = 2$ projections.
The p states in both types of Al are rather similar, but the s
states differ strongly. In particular, the additional Al neighbor
of type 2 Al causes the Al $3s$ states at the Fermi level to form
bonding and antibonding states (indicated in Fig. 2). Type 1 Al
contributes 22% more electronic states at the Fermi level than
type 2 Al. From the electronic structure and the layered crystal
composition in c direction (Figure 1), a rather large anisotropy
in the conductivity tensor is expected.

B. $SrAl_4$ (001) surface

The surface energy of (001) $SrAl_4$ surfaces is calculated
using slab geometry, considering only (001) surfaces since
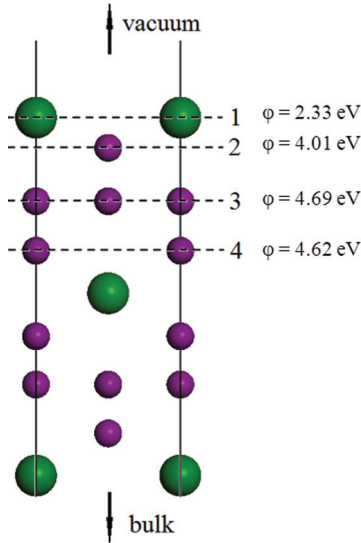
FIG. 3. (Color online) (001) SrAl₄ surface models. The large (small) balls are Sr (Al) atoms. The dashed lines indicate the surface cleavages for our four surface models. The atomic layer on a dashed line faces vacuum. Also shown are the calculated work function values for each surface model.

our measurements indicate this to be the preferred growth orientation of SrAl₄ on LAO substrate. We use 1×1 surface cells and SrAl₄ slabs that are ~15–20 Å thick. Two neighboring slabs are separated by at least 15 Å of vacuum to suppress slab-slab interactions due to the periodic boundary conditions. We show the surface models in Fig. 3. We construct a total of four surface terminations (enumerated from 1 to 4 in the figure) with the following procedure. The dashed lines in Fig. 3 indicate how we cleave each of the four surfaces. The first model is terminated with Sr atoms at the first dashed line, the second to fourth surfaces are terminated with Al as indicated by the second to fourth dashed line. Surfaces 2 and 4 are terminated with type 2 Al; surface 3 is terminated with type 1 Al. When counting all atoms and comparing to the Sr/Al ratio of bulk SrAl₄, then models 1 and 4 are Sr rich, although Al faces vacuum in model 4. Models 2 and 3 are Al rich when compared to the Sr/Al ratio of bulk SrAl₄.

The Gibbs free energy approach is used to estimate the surface energy:[21]

$$\sigma = [E_{\text{slab}} - N_{\text{Al}}(E_{\text{Al}} + \mu_{\text{Al}}) - N_{\text{Sr}}(E_{\text{Sr}} + \mu_{\text{Sr}})]/2A, \quad (1)$$

where E_{slab} is the energy of the slab, N_X is the number of atomic species X (Al or Sr), and μ_x and E_x are its chemical potential and bulk energy, respectively. The chemical potentials are referenced to the bulk energies of metallic Sr and Al. Assuming equilibrium of the surface with the bulk,

$$\mu_{\text{Sr}} + 4\mu_{\text{Al}} = H_f = -1.131 \text{ eV},$$
$$H_f < \mu_{\text{Sr}} < 0, \quad H_f < 4\mu_{\text{Al}} < 0, \quad (2)$$

then (1) can be rewritten as a function of the chemical potential μ_{Sr} solely:

$$\sigma = [E_{\text{slab}} - N_{\text{Sr}}E_{\text{Sr}} - N_{\text{Al}}(E_{\text{Al}} + 0.25H_f)$$
$$- \mu_{\text{Sr}}(N_{\text{Sr}} - 0.25N_{\text{Al}})]/2A, \quad H_f < \mu_{\text{Sr}} < 0. \quad (3)$$

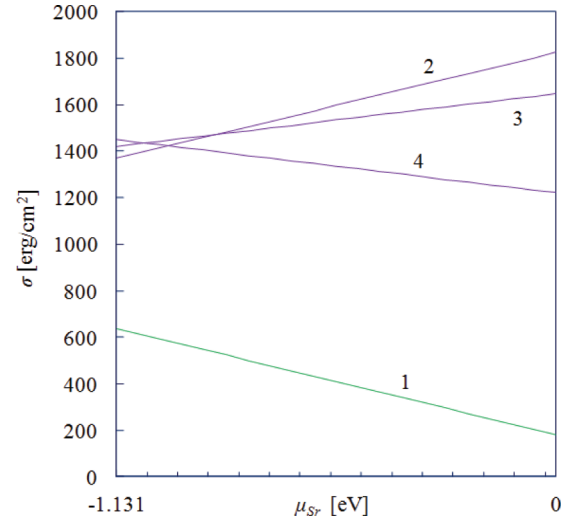
FIG. 4. (Color online) (001) SrAl₄ surface energy for models 1–4. The Sr-terminated model 1 has the lowest surface energy over the entire chemical range, followed by the Al-terminated model 4 with an increase in energy by approximately 1000 erg/cm².

Note that the heat of formation per SrAl₄ unit is 0.343 eV lower than what we found for SrAl₂.[19] The boundary conditions for μ_{Sr} correspond to Sr-poor experimental conditions for $\mu_{\text{Sr}} = H_f$, and Sr-rich conditions for $\mu_{\text{Sr}} = 0$. The surface energies are shown in Fig. 4 and the surface models are indicated in the plot. The surface energy ranges between 200 erg/cm² and 1800 erg/cm² depending on the chemical environment. For comparison, the values for SrAl₂ range from 320 erg/cm² to 1842 erg/cm². Over the entire range of chemical potentials, the Sr-rich surface model has the lowest energy. The next preferable surface is 800 erg/cm² higher in energy than the lowest one. This is important when we consider the wetting behavior of thin SrAl₄ films on LAO in the next paragraph.

For all four surface models, the work function is also calculated. In order to do so, we calculate the plane-averaged electrostatic potential separately in the slab and in the vacuum regions of the simulation cell. We identify the vacuum energy with the potential value deep in the vacuum region of the cell. The difference between the vacuum energy and the Fermi energy is the work function. The work function is indicated in Fig. 3. The values range from 2.34 eV to 4.69 eV. As found for SrAl₂, the exact value is strongly termination dependent.[19] The Sr-terminated surface model has the lowest work function, comparable to the 2.59 eV found for Sr metal. All other models are Al terminated, and thus their work function is rather close to 4.41 eV for bulk Al.

C. LAO/SrAl₄ interface

We consider two interface models for the (001)LAO/(001)SrAl₄ interface shown in Fig. 5. The LAO substrate has AlO₂ termination in both models while the first layer of SrAl₄ facing LAO is Sr in model 1 and Al in model 2. The in-plane lattice vectors of the LAO substrate are along the (2 1 0) and (−1 2 0) axes of the LAO primitive surface cell. The rotation allows for a better match with a 2×2 cell of the primitive SrAl₄ surface by only applying
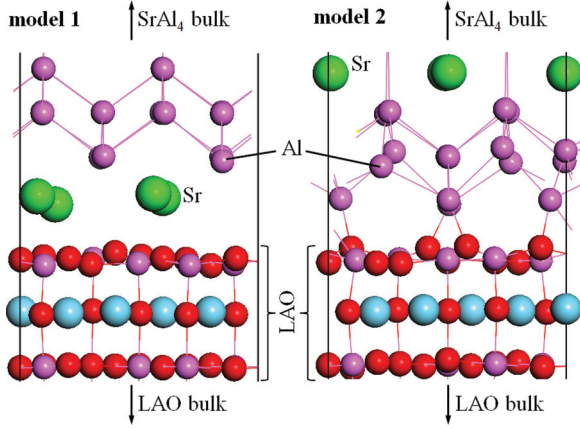
FIG. 5. (Color online) Theoretical models of the LAO/SrAl$_4$ interface. The LAO is $\sim$20 Å thick, followed by an $\sim$20 Å thick metal layer. Model 1 has an Sr layer facing the LAO substrate; in model 2 an Al layer faces the LAO substrate. The pictures show the relaxed structures.

4.5% lateral compressive strain to SrAl$_4$. The LAO is 20 Å thick, followed by approximately 20 Å thick metal layers.

For the SrAl$_4$ layer to wet AlO$_2$-terminated LAO, the following wetting condition must be satisfied:

$$\sigma_{\text{SrAl}_4} + \sigma_i < \sigma_{\text{LAO}}, \qquad (4)$$

where σ_i is the interface energy, σ_{LAO} is the LAO substrate surface energy, and σ_{SrAl_4} is the SrAl$_4$ surface energy. The interface energy σ_i is given by

$$\sigma_i = \left[E_{\text{slab}} - E_{\text{LAO}}^{\text{bulk}} - E_{\text{SrAl}_4}^{\text{bulk}}\right]/2A, \qquad (5)$$

where $E_{\text{LAO}}^{\text{bulk}}$ is the substrate bulk energy and $E_{\text{SrAl}_4}^{\text{bulk}}$ the metal bulk energy. We rewrite the substrate bulk energy as

$$E_{\text{LAO}}^{\text{bulk}} = E_{\text{LAO}}^{\text{bulk}} + 2A\sigma_{\text{LAO}} - 2A\sigma_{\text{LAO}} = E_{\text{LAO}}^{\text{surface}} - 2A\sigma_{\text{LAO}}. \qquad (6)$$

$E_{\text{LAO}}^{\text{surface}}$ is calculated in a separate LAO surface calculation using slab geometry. Using (6) in (5) and rearranging terms we obtain

$$\sigma_i - \sigma_{\text{LAO}} = \left[E_{\text{slab}} - E_{\text{LAO}}^{\text{surface}} - E_{\text{SrAl}_4}^{\text{bulk}}\right]/2A. \qquad (7)$$

Comparing Eq. (7) with (4) we rewrite the wetting condition as

$$\left[E_{\text{slab}} - E_{\text{LAO}}^{\text{surface}} - E_{\text{SrAl}_4}^{\text{bulk}}\right]/2A < -\sigma_{\text{SrAl}_4}. \qquad (8)$$

The first two energies on the left-hand side of Eq. (8) are extracted directly from our VASP calculations; the third energy is evaluated as described in Eqs. (1)–(3) for the SrAl$_4$ surface energy. This leads to the final wetting condition:

$$\left[E_{\text{slab}} - E_{\text{LAO}}^{\text{surface}} - N_{\text{Sr}}E_{\text{Sr}} - N_{\text{Al}}(E_{\text{Al}} + 0.25H_f)\right.$$
$$\left. + \mu_{\text{Sr}}(0.25N_{\text{Al}} - N_{\text{Sr}})\right]/2A < -\sigma_{\text{SrAl}_4}. \qquad (9)$$

The left-hand side of Eq. (9) for two interfaces is shown in Fig. 6 as two thick lines, while the $-\sigma_{\text{SrAl}_4}$ on the right-hand side is shown by thin lines. Whenever the thick lines are smaller than any of the $-\sigma_{\text{SrAl}_4}$ wetting can occur for this combination of interface and SrAl$_4$ surface (the numbers correspond to Fig. 4). In Fig. 6 we see that the Sr-terminated SrAl$_4$ layer
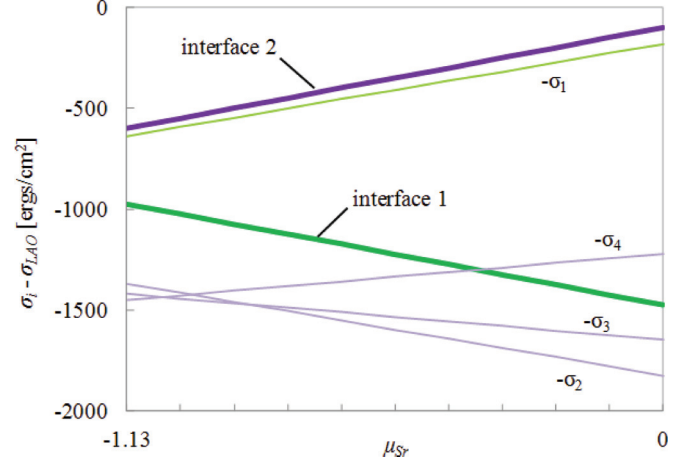

FIG. 6. (Color online) Thick lines in the plot are (σ_i-σ_{LAO}) for interface model 1 and 2 as functions of the chemical potential μ_{Sr}. Also shown is the previously calculated negative surface energy of SrAl$_4$-σ_i as a function of the chemical potential. SrAl$_4$ wets the LAO substrate whenever the value (σ_i-σ_{LAO}) is smaller than one of the negative SrAl$_4$ surface energies $-\sigma_i$.

(line $-\sigma_1$) always satisfies the wetting condition for interface model one, while the Al-terminated SrAl$_4$ layer (lines $-\sigma_2,\sigma_3,\sigma_4$) only wets under Sr-rich conditions for model 4 (this SrAl$_4$ surface has the least amount of Al at the surface). We conclude that wetting is easier to achieve with Sr termination of the aluminide.

Having developed the interface models, we then calculate the Schottky barrier height (SBH) at each interface from the local electrostatic potential. In Fig. 7 we show the in-plane averaged electrostatic potential for the interface model 1, plotted in the z direction. Deep in the LAO region the potential corresponds to that of bulk LAO, and we can place the top of the LAO valence band with respect to the average potential. We obtain the energy difference between the average potential and the valence band top from a separate bulk LAO calculation. The p-type SBH is the energy difference between the Fermi level and the top of the bulk LAO valence band. For interface
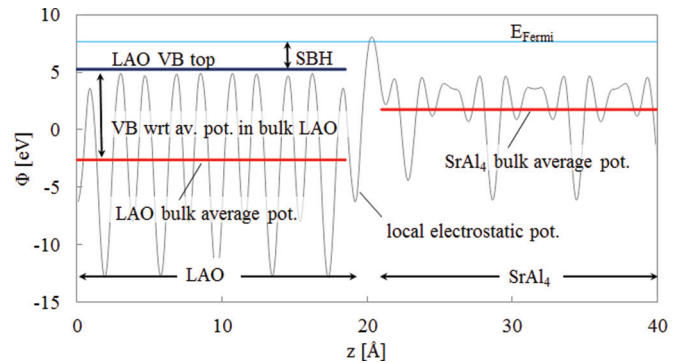

FIG. 7. (Color online) x-y average of the local electrostatic potential in the LAO/SrAl$_4$ supercell along with the Fermi level and the LAO valence band (VB) top. The VB top is set with respect to the average potential deep inside the LAO layer. The energy difference between the average potential and the VB top is extracted from a separate bulk LAO calculation. The SBH is the difference in energy between the Fermi level in the supercell and the LAO VB top.

one, the p-type SBH of 2.34 eV is found (the value of 2.63 eV is obtained for interface 2).

III. GROWTH

The growth of SrAl$_4$ on LAO is carried out in a customized DCA Instruments M600 MBE system with a base pressure of 2×10^{-10} Torr. Al and Sr metal fluxes are introduced to the substrate surface by heating Knudsen effusion cells to predetermined temperatures and controlling the growth through shuttering. The fluxes were calibrated using a quartz crystal microbalance incorporated in the MBE system. Additionally, the entire growth process is monitored *in situ* through a differentially pumped Staib Instruments RHEED gun attached to the growth chamber.

For sample growth, polished (100)-oriented LAO single crystals with dimensions 5 mm $\times$ 5 mm $\times$ 0.5 mm manufactured by CrysTec are used. Below 400 °C, LAO has a rhombohedral perovskite structure (space group $R\bar{3}c$) with lattice constants $a = b = c = 3.788$ Å and angles $\alpha = \beta = \gamma = 90.022°$.[22] LAO undergoes a phase transition to a cubic structure (space group $Pm3m$) at 400 °C.[23] Prior to growth the substrates were annealed in vacuum in the MBE chamber for 15 min at a temperature of 700 °C. The RHEED pattern after annealing showed a 1×1 unreconstructed surface, as shown in Fig. 8(a). Growth of the aluminide film was subsequently initiated at a substrate temperature of 400 °C. The sources were calibrated to yield a thickness of 1.13 Å per min for Al and 3.74 Å per min for Sr, which corresponded to equal fluxes for both materials. The deposition was performed under ultrahigh-vacuum conditions such that the Al shutter was constantly open while the Sr shutter was pulsed, alternately opening the shutter for 19 s and closing it for 20 s. Despite the calibration of the fluxes, this growth process yielded a 1:4 ratio of Sr:Al on the substrate, indicating a reduced

sticking coefficient for Sr at the growth temperature. After the deposition of about 1.5 unit cells of SrAl$_4$, the RHEED pattern from the substrate was no longer visible and the crystalline diffraction pattern of SrAl$_4$ could be identified. RHEED indicated three-dimensional Volmer-Weber growth for SrAl$_4$ as the diffraction streaks were interrupted by spots; the pattern became clearer as the growth was continued [Figs. 8(a)–8(d)]. All samples in this study were grown according to this recipe and films were deposited with thicknesses of up to ~480 Å without any noticeable change in the RHEED pattern.

After growth, the samples were cooled down to room temperature and transferred *in situ* to the XPS/UPS system via a vacuum buffer line. *Ex situ* x-ray diffraction (XRD), atomic force microscopy (AFM), transmission electron microscopy (TEM), and dc conductivity measurements in the van der Pauw geometry were then performed as described below.

IV. RESULTS AND DISCUSSION

Typical RHEED patterns of the thin SrAl$_4$ films are shown in Figs. 8(c) and 8(d). Two different spacings can be identified with the $\langle 100 \rangle$ and the $\langle 110 \rangle$ directions of the (001) SrAl$_4$ surface. The in-plane lattice constants of the film can be calculated assuming an in-plane lattice constant of $a_{\text{LAO},\langle 100 \rangle} = 3.788$ Å in Fig. 8(a). The measured in-plane spacings for the film are $a_{\text{SrAl}_4,\langle 110 \rangle} = 3.14$ Å and $a_{\text{SrAl}_4,\langle 100 \rangle} = 4.43$ Å in excellent agreement with the lattice constant reported in the literature $a_{\text{SrAl}_4,\langle 100 \rangle} = 4.461$ Å,[16] indicating a nearly unstrained film. All samples exhibited spotty features in RHEED indicating 3D scattering of the electrons that could be attributed to large surface step heights. The RHEED pattern shows two different film orientations in epitaxial registry to the substrate: $\langle 110 \rangle_{\text{SrAl}_4} // \langle 110 \rangle_{\text{LAO}}$ and $\langle 100 \rangle_{\text{SrAl}_4} // \langle 110 \rangle_{\text{LAO}}$. Furthermore, no significant change in the RHEED patterns was seen when the growth temperature was varied between 400 °C and 800 °C.

Symmetric 2θ-θ x-ray diffraction measurements were carried out *ex situ* to obtain the out-of-plane lattice constant. The scan shown in Fig. 9 reveals an out-of-plane lattice spacing of $n \times 5.59$ Å and a substrate spacing of $n \times 3.77$ Å. Comparing this value to all known stable phases of the Sr-Al system,[24] there is excellent agreement solely with the (001) orientation of the SrAl$_4$ lattice $c_{\text{SrAl}_4,\langle 001 \rangle} = 11.209$ Å,[16] while the absence of other peaks confirms the pure (001) orientation of the unstrained epitaxial film.

Figure 10 shows an *ex situ* AFM image of a sample after growth of about 11 unit cells of SrAl$_4$. Rectangular islands of different heights are clearly visible over the 2 μm $\times$ 2 μm area. The median island width is on the order of 0.2 μm, also seen from the spectral distribution maximum of the Fourier transform of the surface image ($\sim 10^{-2.3}$ nm^{-1}). The island heights vary in the range 5 to 25 nm, indicating step heights greater than several unit cells. The root mean square over heights measured is in the range of 6–8 nm, independent of deposition time. It is interesting to note that neither the substrate growth temperature nor the deposition time greatly altered the island shape and size. These results confirm the three-dimensional Volmer-Weber growth mode suggested by RHEED. Furthermore, another structure of the film on the order of 0.1 mm was visible under an optical microscope
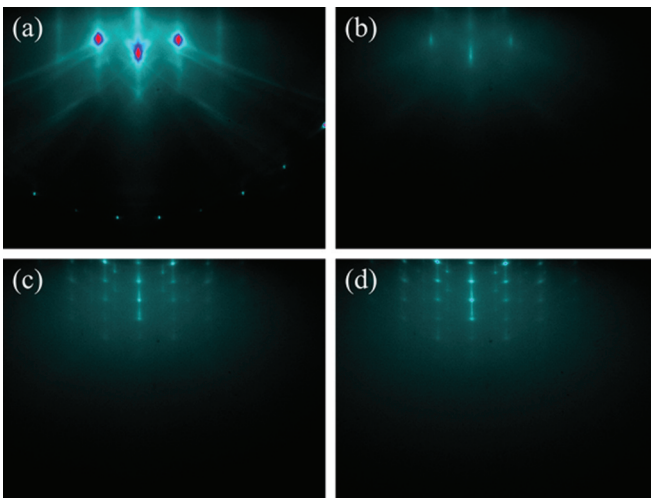

FIG. 8. (Color online) RHEED patterns of the sample surface during growth recorded along the $\langle 110 \rangle$ direction of LaAlO$_3$ using 18-keV electrons: (a) clean LAO surface; (b)–(d) SrAl$_4$ after growth of 1.5 (b), 3 (c), and 7 (d) unit cells of SrAl$_4$. The spots indicate substantial step heights on the surface. Two different spacings corresponding to the $\langle 110 \rangle$ and the $\langle 100 \rangle$ directions of the SrAl$_4$ surface can be observed.
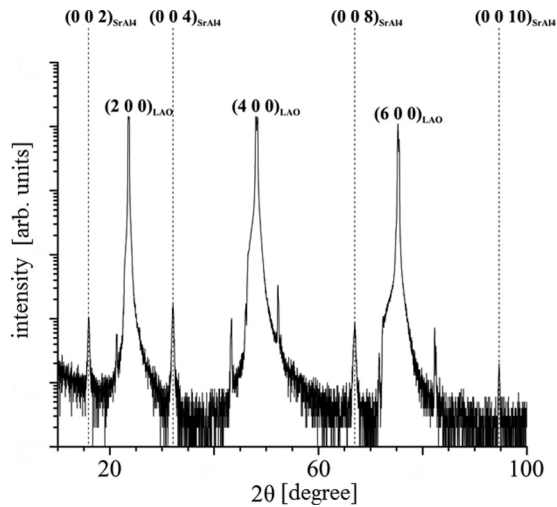
FIG. 9. Typical XRD θ-2θ scan of a 16-nm-thick SrAl$_4$ film showing preferred (001) orientation. The unlabeled peaks near the LAO substrate peaks are from the substrate as confirmed from a measurement of a bare substrate.

(not shown). This structure, however, is related to the topography of the LAO substrate as a result of twinning.[25]

The Volmer-Weber growth mode was also confirmed by *ex situ* TEM characterization, with electron micrographs showing the existence of islands as suggested by AFM and RHEED. Figure 11 shows a cross-sectional TEM image of such an island of thin SrAl$_4$ grown according to the above described recipe and capped with 4 nm of polycrystalline Ge

FIG. 10. (Color online) AFM image of the surface of 25 nm SrAl$_4$ deposited on LAO (top) alongside plots of the spectral distribution of the Fourier transform of the surface image (lower left) and a height distribution (lower right).
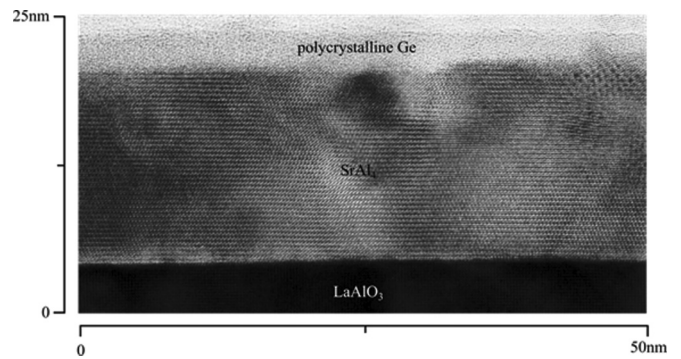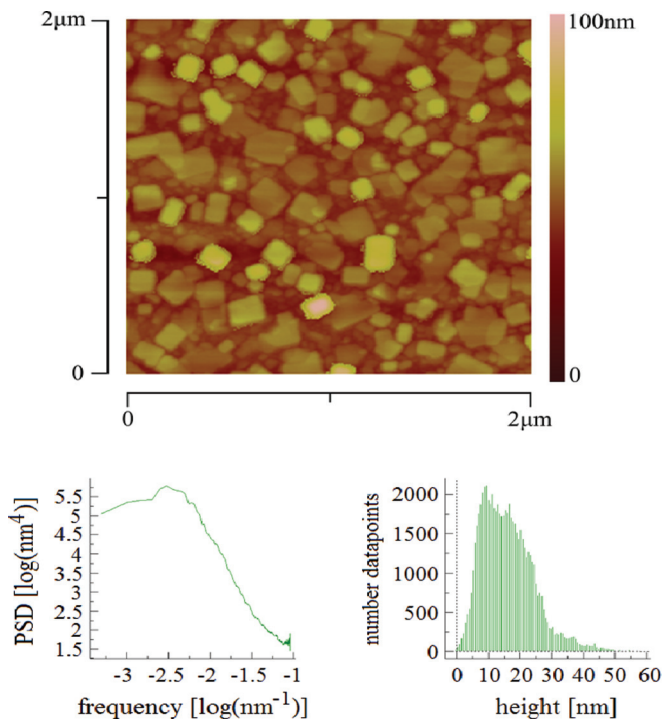

FIG. 11. Cross-sectional TEM image of 16-nm-thick crystalline SrAl$_4$ on (100) oriented LAO capped with 4 nm of polycrystalline germanium.

to prevent interaction with air. The SrAl$_4$ island shows epitaxial registry with the substrate and a high degree of crystallinity.

For x-ray photoelectron spectroscopy of the samples, it is necessary to work around the problem of charging effects due to the insulating LAO substrate. For this purpose, the LAO substrate was bonded onto heavily *p*-doped silicon, while at the same time creating a conducting channel from the Si surface to the LAO surface by means of Ag paste. Subsequently, *in situ* XPS and UPS were performed on SrAl$_4$/LAO samples using a VG Scienta MX 650 monochromated Al K_α (1486.7 eV) x-ray source and a VG Scienta VUV 5000 ultraviolet light source utilizing the He I (21.22 eV) line, without observing any charging effects. In addition to the energy level of Al atoms in the LAO lattice, the recorded XPS spectra of the Al $2p$ core level in Fig. 12 show another core level at 72.67 eV that can be attributed to Al $2p_{3/2}$ in the SrAl$_4$ lattice. When fitting Al core levels with symmetric Gaussian or Lorentzian functions, an additional peak needs to be introduced to account for the natural asymmetry in metallic Al.[26] Although one might expect two distinct Al $2p$ core levels for the SrAl$_4$ lattice due to the slightly different chemical environments, only one level for both types of Al could be resolved. The Sr $3d$ spectrum in Fig. 12 lies at an energy of 133.44 eV for the $3d_{5/2}$ level and is overlapped with a plasmon feature from aluminum.[27] XPS core level binding energies are conventionally referenced to the Fermi level of the spectrometer due to the experimental setup.

To determine the true chemical shift of elements with respect to their bulk values in different materials, the measured binding energy values must be referenced to the vacuum level by adding the work function of the material. Thus the work function of bulk SrAl$_4$ can be determined in the (001) direction by UPS analysis of the electron energy cutoff using a sample in which no photoelectrons of the LAO substrate were detectable. The work function of SrAl$_4$ was found to be $\phi_{(001)} = 3.05$ eV. Hence the chemical shifts of the Al $2p_{3/2}$ level and the Sr $3d_{5/2}$ level in SrAl$_4$ can be obtained with respect to their measured values in polycrystalline Al metal (72.75 eV) and polycrystalline Sr metal (134.28 eV) and are found to be $\Delta_{Al} = -1.36$ eV and $\Delta_{Sr} = -0.38$ eV, where a negative value means a shift to lower binding energies. This can be interpreted as confirmation of SrAl$_4$ as a Zintl phase: Sr donates electrons to Al, which assumes, at least
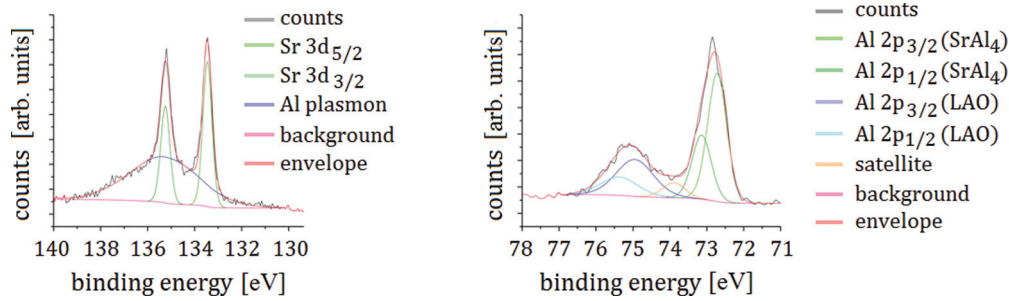
FIG. 12. (Color online) XPS spectra of Sr $3d$ core level (left) and Al $2p$ core level (right) of a 12-nm-thick $SrAl_4$ film grown on LAO.

partly, a structure with four nearest neighbors in a tetrahedral arrangement, with the additional electron lowering the binding energy of the Al core levels.

The valence band offset between $SrAl_4$ and LAO was also measured using XPS. The schematic of the measurement is shown in Fig. 13. The positions of the La $3d_{5/2}$ level and the valence band maximum of LAO were measured using a bulk single crystal of LAO. The valence band maximum was determined using the linear extrapolation method.[28] The energy difference between these two levels was found to be 832.0 eV. The positions of the Fermi level and the Sr $3d_{5/2}$ core level of $SrAl_4$ were then determined from a thick ($\sim$16 nm) film of $SrAl_4$ grown on LAO. The Fermi level position was taken as the midpoint of the measured Fermi edge spectrum. The energy difference between these two levels was found to be 131.8 eV. Finally, a thin ($\sim$8 nm) film of $SrAl_4$ on LAO was grown and the separation between the La $3d_{5/2}$ and Sr $3d_{5/2}$ levels was determined. The energy difference was measured to be 702.4 eV. From these three energy differences, the valence

FIG. 13. (Color online) Schematic energy band diagram of energy levels used in the XPS valence band offset determination between LAO and $SrAl_4$.

band offset is calculated to be 2.2 ± 0.2 eV with the Fermi level of $SrAl_4$ above the valence band top of LAO. The main source of error comes from the uncertainty in positioning the valence band top using the linear extrapolation method. The measured valence band offset is in excellent agreement with the theoretical value of 2.34 eV for the model structure with the Sr layer at the interface.

The island morphology of the $SrAl_4$ may be related to the instability of the LaO-terminated $LAO/SrAl_4$ interface and the mixed termination of the LAO surface. Comparison of the work function calculations with the measured value of 3.05 eV suggests that the surfaces of the $SrAl_4$ films are primarily Sr terminated, with possibly some intermixed Al termination. The calculations also suggest that this corresponds to the lowest energy $SrAl_4$ surface. The surface termination of LAO is reported to be temperature dependent, being exclusively AlO_2 terminated below approximately 150 °C and LaO terminated above 250 °C after annealing periods exceeding 8 h with temperatures above 800 °C.[29] More recent studies suggest both terminations at room temperature with purely La-O termination at temperatures above 727 °C.[30] While our growth is carried out at a temperature well above 250 °C, we have not independently determined the termination of our LAO substrates, and since annealing periods in this work are relatively short and only at 700 °C, it is possible that our LAO surface has mixed termination. From our DFT calculations, we see that wetting is possible for Sr-terminated $SrAl_4$ on AlO_2-terminated LAO. The observed island growth possibly arises from growth on a mixed termination LAO surface, with the aluminide islands growing preferentially over patches of AlO_2-terminated LAO, as theoretically predicted. The close agreement between the theoretical Schottky barrier height of 2.3 eV and experimental valence band offset of 2.2 eV lends further support to this hypothesis.

The transport properties of $SrAl_4$ films were investigated over a wide temperature range from 2.3 K to 300 K. The temperature dependence of the resistivity and Hall resistivity of a 70-nm-thick $SrAl_4$ film on LAO were measured in magnetic fields up to 8 T applied perpendicular to the film plane. The measurements were done in a standard van der Pauw geometry with four contact probes located at the corners of a 5-mm-square sample. The temperature dependence of the in-plane resistivity [Fig. 14(a)] shows the expected behavior for metals with a room temperature value of ρ_{SrAl_4}(300 K) = 45.2 $\mu\Omega$ cm, dropping linearly until 75 K with a decreasing slope afterwards approximately following a T^2 dependence, which suggests a large contribution from electron-electron
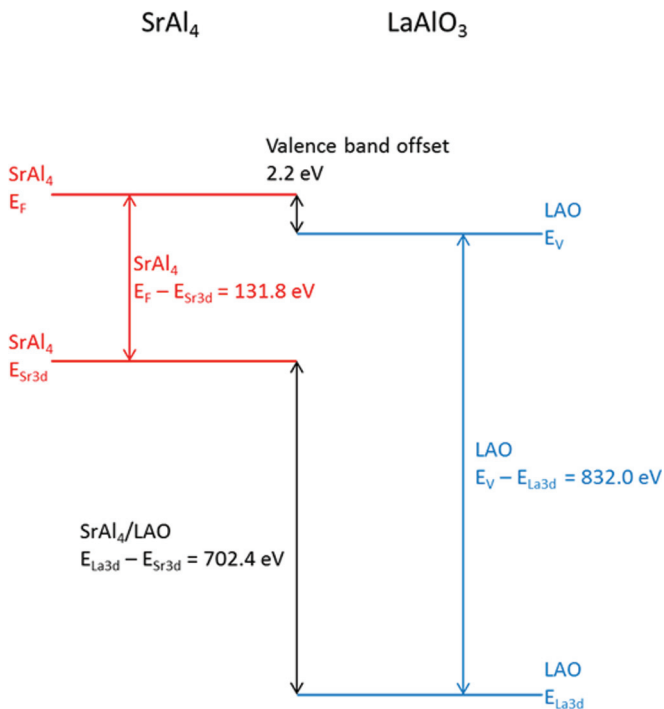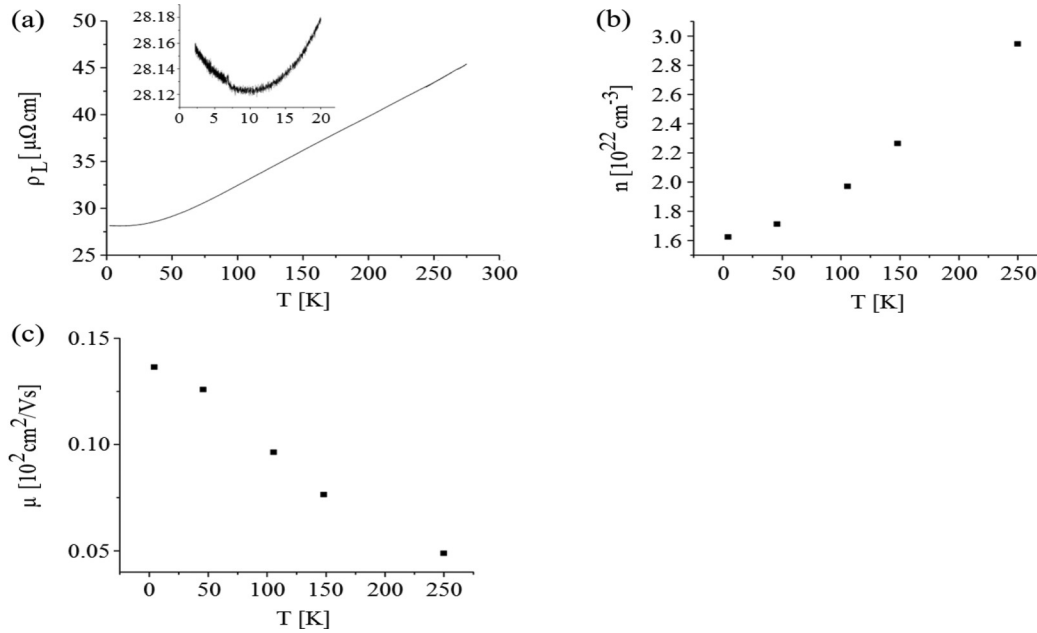
FIG. 14. (a) Resistivity, (b) carrier density, and (c) mobility of a 70-nm-thick SrAl$_4$ slab is measured in the temperature region from 2.3 to 300 K.

scattering. However, the resistivity around 10 K shows a global minimum in the measured temperature region, which may be due to correlation or possibly disorder effects, but is beyond the scope of this study. The room temperature carrier density is $n_{SrAl_4}(300 \text{ K}) = 3.29 \times 10^{22} \text{ cm}^{-3}$ while the room temperature mobility is 4.19 cm^2/V s, as determined from the Hall resistivity. Furthermore, the material also exhibits positive magnetoresistance (not shown). The carrier density obtained by integrating the theoretical density of states over the conduction band amounts to roughly $n_{SrAl_4}(300 \text{ K}) = 1.0 \times 10^{23} \text{ cm}^{-3}$, which is about three times larger than the measured value. This discrepancy might result from the high degree of film roughness. The real film thickness may vary significantly over the film area compared to the nominal value, which could reduce the carrier density value calculated from Hall measurements.

V. SUMMARY

We have studied thin films of SrAl$_4$ grown by MBE on (100)-oriented LAO substrates and characterized structural and electrical properties of the thin aluminide film. RHEED,

XRD, and TEM demonstrated the epitaxial Volmer-Weber growth mode of an unstrained, (001)-oriented SrAl$_4$ film with a mean island size of $\sim$0.2 μm. Optimal results for crystalline structure and composition were achieved with a pulsed evaporation technique. XPS analysis confirmed electron transfer into aluminum in the Zintl-Klemm sense, with a chemical shift to lower binding energies. Comparison of the experimental work function of $\phi_{(001)} = 3.05$ eV with DFT calculations suggested that the surface was mostly Sr terminated. Experimental determination of the band offset like-wise shows excellent agreement with the suggested interface model. Transport properties showed behavior consistent with the expected semimetallic nature of the material.

*demkov@physics.utexas.edu

[1]E. Zintl, Z. Phys. Chem. **154**, 1 (1931).

[2]T. F. Faessler, *Zintl Phases: Principles and Recent Developments* (Springer, Berlin, 2011).

[3]G. J. Snyder and E. S. Toberer, Nat. Mater. **7**, 105 (2008).

[4]R. J. Cava, H. Ji, M. K. Fuccillo, Q. D. Gibson, and Y. S. Hor, arXiv:1302.1059 [cond-mat.mtrl-sci].

[5]A. A. Demkov, H. Seo, X. Zhang, and J. Ramdani, Appl. Phys. Lett. **100**, 71602 (2012).

[6]J. W. Reiner, A. M. Kolpak, Y. Segal, K. F. Garrity, S. Ismail-Beigi, C. H. Ahn, and F. J. Walker, Adv. Mater. **22**, 2919 (2010).

[7]X. Zhang, A. A. Demkov, H. Li, X. Hu, Y. Wei, and J. Kulik, Phys. Rev. B **68**, 125323 (2003).

[8]L. Largeau, J. Cheng, P. Regreny, G. Patriarche, A. Benamrouche, Y. Robach, M. Gendry, G. Hollinger, and G. Saint-Girons, Appl. Phys. Lett. **95**, 011907 (2009).

[9]N. A. Bojarczuk, M. Copel, S. Guha, V. Narayanan, E. J. Preisler, F. M. Ross, and H. Shang, Appl. Phys. Lett. **83**, 5443 (2003).

[10]H. J. Osten, A. Laha, M. Czernohorsky, E. Bugiel, R. Dargis, and A. Fissel, Phys. Status Solidi A **205**, 695 (2008).

[11]R. Dargis, A. Fissel, D. Schwendt, E. Bugiel, J. Krügener, T. Wietler, A. Laha, and H. J. Osten, Vacuum **85**, 523 (2010).

[12]R. A. McKee, F. J. Walker, and M. F. Chisholm, Phys. Rev. Lett. **81**, 3014 (1998).

[13]A. A. Demkov and X. Zhang, J. Appl. Phys. **103**, 103710 (2008).

[14]M. Aljarraha, M. A. Parveza, J. Lib, E. Essadiqib, and M. Medraja, Sci. Technol. Adv. Mater. **8**, 237 (2007).

[15]D. Zhou, J. Liu, and P. Peng, Trans. Nonferrous Met. Soc. China **21**, 2677 (2011).

[16]S. Göbel, M. Somer, W. Carrillo-Cabrera, E. M. Peters, K. Peters, and H. G. von Schnering, Z. Kristallogr. **211**, 189 (1996).

[17]J. P. Perdew, K. Burke, and M. Ernzerhof, Phys. Rev. Lett. **77**, 3865 (1996).

[18]G. Kresse and J. Hafner, Phys. Rev. B **47**, 558 (1993); G. Kresse and J. Furthmüller, Comput. Mater. Sci. **6**, 15 (1996); Phys. Rev. B **54**, 11169 (1996); G. Kresse and J. Hafner, J. Phys.: Condens. Matter **6**, 8245 (1994); G. Kresse and D. Joubert, Phys. Rev. B **59**, 1758 (1999).

[19]A. Slepko and A. A. Demkov, Phys. Rev. B **85**, 195462 (2012).

[20]H. J. Monkhorst and J. D. Pack, Phys. Rev. B **13**, 5188 (1976).

[21]G.-X. Qian, R. M. Martin, and D. J. Chadi, Phys. Rev. B **38**, 7649 (1988).

[22]G. W. Berkstresser, A. J. Valentino, and C. D. Brandle, J. Cryst. Growth **109**, 467 (1991).

[23]J. Yao, P. B. Merrill, S. S. Perry, D. Marton, and J. W. Rabalais, J. Chem. Phys. **108**, 1645 (1998).

[24]S. Srikanth and K. T. Jacob, Z. Metallkd. **82**, 675 (1991).

[25]S. A. Hayward, S. A. T. Redfern, and E. K. H. Salje, J. Phys.: Condens. Matter **14**, 10131 (2002).

[26]S. Doniach and M. Sunjic, J. Phys. C: Solid State Phys. **3**, 285 (1970).

[27]J. F. Moulder, W. F. Stickle, P. E. Sobol, and K. D. Bomben, in *Handbook of X-ray Photoelectron Spectroscopy*, edited by J. Chastain and R. C. King, Jr., (Physical Electronics, Inc., Eden Prairie, 1995).

[28]S. A. Chambers, T. Droubay, T. C. Kaspar, and M. Gutowski, J. Vac. Sci. Technol. B **22**, 2205 (2004).

[29]J. P. Jacobs, M. A. San Miguel, and L. J. Alvarez, J. Mol. Struct. **390**, 193 (1997).

[30]H. Kawanowa, H. Ozawa, M. Ohtsuki, Y. Gotoh, and R. Souda, Surf. Sci. **506**, 87 (2002).